ResearchGate

See discussions, stats, and author profiles for this publication at: https://www.researchgate.net/publication/282558601

Dynamic crashing behavior of new extrudable multi-cell tubes with a functionally graded thickness

Article *in* International Journal of Mechanical Sciences · November 2015

DOI: 10.1016/j.ijmecsci.2015.08.029

CITATIONS
200

READS
734

5 authors, including:

Jianguang Fang
University of Technology Sydney
127 PUBLICATIONS **6,111** CITATIONS

SEE PROFILE

Yunkai Gao
Tongji University
58 PUBLICATIONS **2,018** CITATIONS

SEE PROFILE

Guangyong Sun
Hunan University
257 PUBLICATIONS **16,509** CITATIONS

SEE PROFILE

Gang Zheng
Hunan University
39 PUBLICATIONS **1,852** CITATIONS

SEE PROFILE

All content following this page was uploaded by Guangyong Sun on 10 May 2021.

The user has requested enhancement of the downloaded file.

International Journal of Mechanical Sciences 103 (2015) 63–73

Contents lists available at ScienceDirect

International Journal of Mechanical Sciences

journal homepage: www.elsevier.com/locate/ijmecsci

Dynamic crashing behavior of new extrudable multi-cell tubes with a functionally graded thickness

Jianguang Fang [a,c], Yunkai Gao [a], Guangyong Sun [b,c,*], Gang Zheng [b], Qing Li [c,**]

[a] School of Automotive Studies, Tongji University, Shanghai 201804, China
[b] State Key Laboratory of Advanced Design and Manufacture for Vehicle Body, Hunan University, Changsha 410082, China
[c] School of Aerospace, Mechanical and Mechatronic Engineering, The University of Sydney, Sydney, NSW 2006, Australia

ARTICLE INFO

Article history:
Received 5 January 2015
Received in revised form
14 August 2015
Accepted 25 August 2015
Available online 14 September 2015

Keywords:
Functionally graded thickness
Extruded multi-cell tube
Crashworthiness
Multiobjective optimization

ABSTRACT

Multi-cell structures have been extensively studied for their outstanding performance as potential energy absorbers. Unlike existing multi-cell tubes with a uniform thickness (UT), this paper introduces a functionally graded thickness (FGT) to multi-cell tubes under dynamic impact, which can be fabricated by an extrusion process. A numerical model is first established using the nonlinear finite element analysis code LS-DYNA and validated with experimental data. Based on a numerical study, the thickness gradient parameters in different regions have considerable effects on the crashworthiness of the FGT multi-cell tubes. Moreover, the FGT multi-cell tubes are able to absorb more energy while yielding a similar level of peak impact force to the UT multi-cell tubes. Finally, multiobjective optimizations of the UT and FGT multi-cell tubes are then performed to determine the optimal gradient parameters that simultaneously improve the specific energy absorption (SEA) and reduce the maximum impact force. In these optimizations, the multiobjective particle optimization (MOPSO) algorithm and response surface (RS) surrogate modeling technique are adopted. The optimization results demonstrate that the FGT multi-cell tubes produce more competent Pareto solutions than the conventional UT counterparts; similar gradients in the outer walls and stronger internal ribs are recommended for the FGT multi-cell tubes because of their improved interactions.

© 2015 Elsevier Ltd. All rights reserved.

1. Introduction

In automotive engineering, thin-walled structures have been extensively used because of their exceptional performance in energy absorption and their light weight. Fig. 1 displays a typical front longitudinal rail [1], which is responsible for absorbing approximately 50% of the kinetic energy of the vehicle during a full frontal collision [2]. The forward part of the rail structure is generally straight to induce progressive folding collapse in the axial direction; this is regarded as the most efficient deformation mode for energy absorption. Because the crashing process determines the acceleration pulse of the occupant compartment, which is closely associated with occupant injuries, a crash analysis of the thin-walled structure is considered critically important. In this regard, the earliest research traces back to the 1960s, when Alexander [3] studied axial crushing of cylindrical tubes and developed a closed-form analytical solution for evaluating the average crushing force. Since then, a series of experimental and theoretical studies [4–9] have been performed in this attractive field to investigate square and circular tubes subjected to static and dynamic loads.

Typically, severe deformation with combined bending and membrane deformation occurs near the corners of the tubes [10]. Thus, the number of corner elements on a tube's cross-section largely influences the energy absorption and crashing behaviors [4,11]. One way to enhance the crashworthiness of a frame is to devise sophisticated multi-cells and internal webs [10,12–14]. Another way is to place more material and increase the wall thickness in the corners because these regions undergo more severe deformation; this solution allows for more energy to be absorbed. With this concept in mind, the European Aluminum Association [15] found that a square tube with reinforced corners offered a significantly higher specific energy absorption than a tube with constant wall thickness (as shown in Fig. 2). Zhang et al. [16] investigated square tubes with graded thicknesses and found a 30–35% increase in energy absorption efficiency. The possibility for tailoring wall thickness variations offers a new opportunity for

* Corresponding author. Tel.: +86 731 8881 1445; fax: +86 731 8882 2051.
** Corresponding author. Tel.: +61 2 9351 8607; fax: +61 2 9351 7060.
E-mail addresses: fangjg87@gmail.com (J. Fang), sgy800@126.com (G. Sun), qing.li@sydney.edu.au (Q. Li).

http://dx.doi.org/10.1016/j.ijmecsci.2015.08.029
0020-7403/© 2015 Elsevier Ltd. All rights reserved.

optimization. In other words, this novel configuration enables a more flexible design to achieve better performance.

It is noted that the concept of varying the wall thickness in the longitudinal direction has recently been proposed for enhancing crashworthiness. Sun and his co-workers first explored the tubes with functionally graded thickness (FGT) and found such a FGT tube does outperform the uniform counterpart in crashworthiness subjected to axial crushing [17] and lateral bending [18]. Zhang et al. [19] also investigated the axial crushing of tapered circular tubes with graded thickness that were successfully fabricated using a tube tapering machine. While the FGT structures in the longitudinal direction have demonstrated advantages in crashworthiness, the fabrication process could necessitate some specially dedicated equipment.

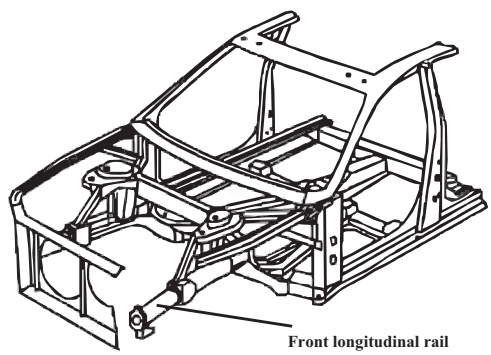

Fig. 1. Front longitudinal rails of the body structure [1].

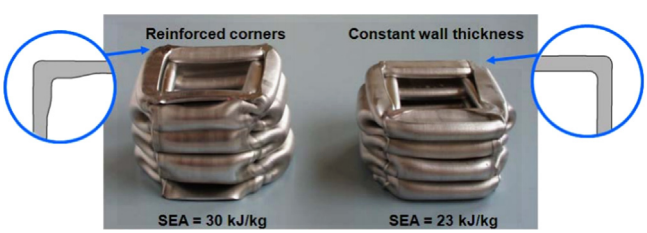

Fig. 2. Corner-reinforced tube vs. uniform wall tube [25].

From a manufacturing perspective, the extrusion process makes it possible to fabricate various prismatic tubes with almost any cross-sections in a cost-efficient manner, not to mention multi-cell and thickness variation configurations. The question is what is the crashworthiness of tubes if these two configurational features are integrated together? Therefore, this study aims to explore the crashworthiness of FGT based multi-cell tubes.

For the crashworthiness problems that involve highly nonlinear contact-impact and large deformation mechanics, analytical objective functions of *SEA* and F_{max} are difficult to derive mathematically. Alternatively, metamodels or surrogate models have been widely utilized to approximate responses during optimization [17,20–25]. Of the various metamodels, the response surface model (RSM) with different orders of polynomial basis functions is the simplest and most commonly used formula and has been successfully used for some crashworthiness optimization problems [26–30]. In this study, the finite element (FE) model of this novel structure is first constructed in LS-DYNA for bearing a dynamic impact loading. The crashworthiness of the FGT multi-cell tubes is then analyzed and compared with that of uniform counterparts based on the RSM. Finally, the multiobjective particle swarm optimization (MOPSO) algorithm is used to optimize the sectional parameters to simultaneously enhance the specific energy absorption (*SEA*) and decrease the maximum crushing force (F_{max}).

2. Numerical modeling

2.1. Geometric description

The structure analyzed is a five-cell tube with a functionally graded wall thickness (Fig. 3a). The length of this tube is $H = 200$ mm,

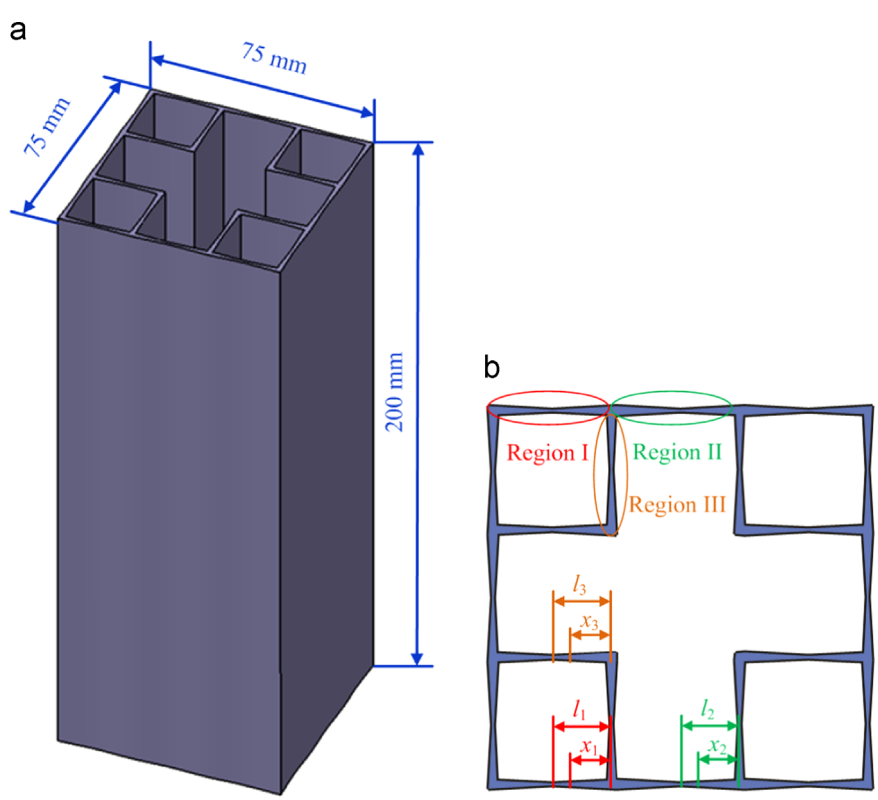

Fig. 3. Configuration of the FGT multi-cell tube: (a) 3D view and (b) 2D cross-sectional view.

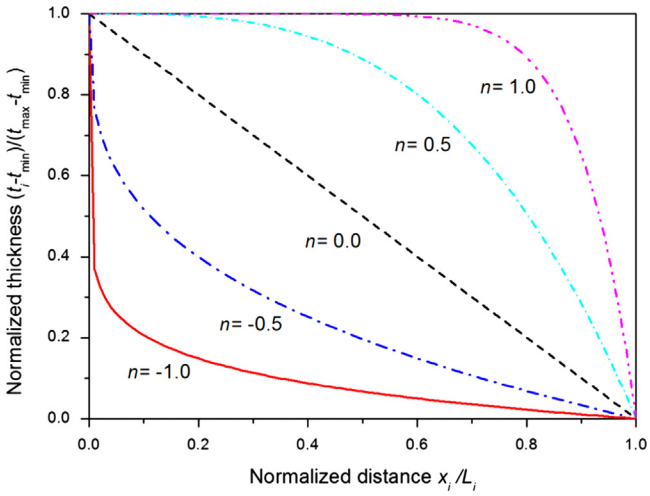

Fig. 4. Thickness variation versus normalized distance.

and its cross-section dimension is $L \times L = 75$ mm $\times$ 75 mm. Fig. 3b depicts the graded thickness configuration in a cross section. Due to geometric symmetry, the cross section is defined for three characteristic regions in this study: exterior walls of the corner-cells (Region I), exterior wall of the middle connector of the corner cells (Region II) and inner ribs (Region III). Thus, the total numbers of these characteristic regions in the FGT tube are eight, four and eight, respectively. Each region is self-symmetric and assumed to have its own thickness gradient as follows:

$$t_i(x_i, n_i) = = t_{max} - (t_{max} - t_{min})\left(\frac{x_i}{l_i}\right)^{10^{n_i}}, \qquad i = 1, 2, 3 \tag{1}$$

where t_{min} and t_{max} are the minimum and maximum wall thicknesses, respectively. In this study, $t_{min} =$ 0.7 mm and $t_{max} =$ 2.0 mm are adopted. x_i and l_i are the distances shown in Fig. 3b. n_i denotes the corresponding normalized gradient parameter that governs the thickness variation $(-1 \le n_i \le 1)$. Thus, Fig. 4 shows the thickness variation versus the normalized distance for different values of n_i. The thickness decreases as x_i increases and the gradient function changes from convex to concave while n_i varies from negative to positive.

2.2. Finite element (FE) model

Finite element models were created to investigate the crashworthiness of these multi-cell tubes (as shown in Fig. 5a). The tube was loaded using a rigid mass block weighing 263 kg with an initial axial velocity of 10 m/s. To initiate a stable and progressive crushing, artificial triggers should be introduced to the FE models. The shape of the triggers on the corner-cell regions and connecting walls near the distal end are illustrated in Fig. 5b. The triggers are placed at a certain distance from the distal end of the tube, which is approximately the half wavelength of one fold, and the depths of the triggers are set to 0.2 mm.

In this study, numerical models were developed using the explicit non-linear finite element code LS-DYNA [31]. Belytschko–Lin–Tsay shell elements [32] with five integration points through the thickness were employed to model the tubes. To model the thickness variation more realistically, different thicknesses were assigned to each of the four nodes of the shell elements based on Eq. (1). A stiffness-based hourglass control was employed to avoid spurious zero energy deformation modes and reduced integration was used to avoid volumetric locking. A rigid wall was used to model the interaction between the impacting mass block and tube (Fig. 6). The interface between the tube and rigid support was modeled as an "automatic node to surface" contact. An "automatic single surface" contact was assigned to the tube to avoid interpenetration during folding deformation. The static and dynamic frictional coefficients were set to 0.3 and 0.2, respectively [33].

The tube was modeled as a piecewise linear elastic–plastic behavior with strain hardening (material model 24 in LS-DYNA). The thin wall material was the aluminum alloy AA6063-T5 with a density of $\rho = 2700$ kg/m^3, Poisson's ratio of $\nu = 0.3$ and Young's modulus of $E = 70$ GPa. The material model was considered insensitive to the strain rate [34] and defined as having non-linear isotropic work hardening in the plastic region. The von Mises yield criterion was used

$$\phi = J_2 - \frac{\sigma_y^2}{3} \tag{2}$$

where the second stress invariant J_2 is defined in terms of the deviatoric stress components as

$$J_2 = \frac{1}{2} s_{ij} s_{ij} \tag{3}$$

and the yield stress σ_y can be defined as

$$\sigma_y = \sigma_0 + f_h\left(\varepsilon_{eff}^p\right) \tag{4}$$

where σ_0 is the initial yield stress and $f_h(\varepsilon_{eff}^p)$ is the hardening function. A uniaxial tensile test was conducted to acquire the hardening function $f_h(\varepsilon_{eff}^p)$. The tensile specimen had an extruded profile with a thickness of 1.5 mm. Fig. 6 shows two experimental curves, i.e., the engineering stress S versus engineering strain e curve and the true stress σ_y versus true strain ε curve. σ_y and ε can be calculated using Eq. (5), and then the true strain ε can be converted to effective plastic strain using

$$\begin{cases} \sigma_y = S(1+e) \\ \epsilon = \ln(1+e) \end{cases} \tag{5}$$

$$\varepsilon_{eff}^p = \varepsilon - \frac{\sigma_y}{E} \tag{6}$$

To determine the size of the elements, a convergence test was performed to minimize the effect of mesh refinement on the accuracy of the numerical analysis, thereby maintaining a reasonable balance with computational cost. The shell element size of 2×2 mm^2 was found to be sufficient to simulate the multi-cell tubes, which were used throughout the present study.

2.3. Validation of the FE modeling

Because the FGT multi-cell tube is a newly introduced structure, an FE model of it cannot be directly validated because of inadequate experimental data because no physical specimen is available for testing. Nevertheless, the FGT multi-cell tube becomes a conventional multi-cell tube with a uniform thickness wall when $t_{min} = t_{max}$ in Eq. (1). It is therefore possible to validate the modeling results in this special case. Fig. 7 shows the drop-hammer impact testing. Fig. 8a and b display the deformation patterns of the two specimens, and Fig. 8c presents the FEA results for the same impact conditions. As shown in these pictures, these four corner-celled regions and the connecting walls of the multi-cell tube undergo inextensional deformation. Note that because no fracture was observed during the dynamic crashing of the physical specimens, the fracture criterion was excluded in the simulation. As expected, the first fold starts from the dedicated triggers and then follows the successive folds. Clearly, the simulated collapse modes are almost the same as those obtained by the experimental tests.

Fig. 9 shows the correlation of the force–displacement response between the experiment and simulation. It is found that the crashing force of the FE prediction follows the same trend as the experimental data. The crashing force in the FE simulation exhibits a lower value in

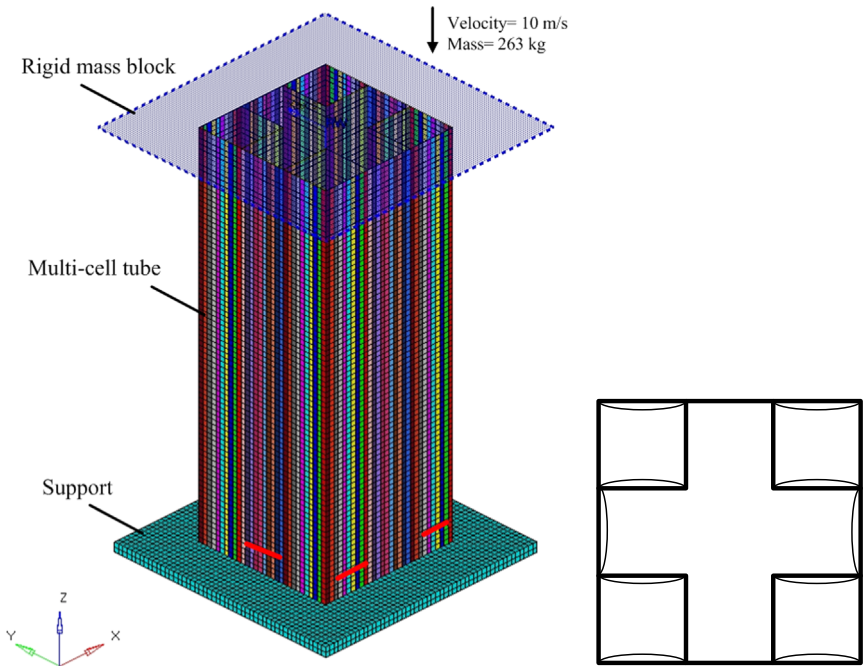

Fig. 5. Finite element model of the FGT multi-cell tube.

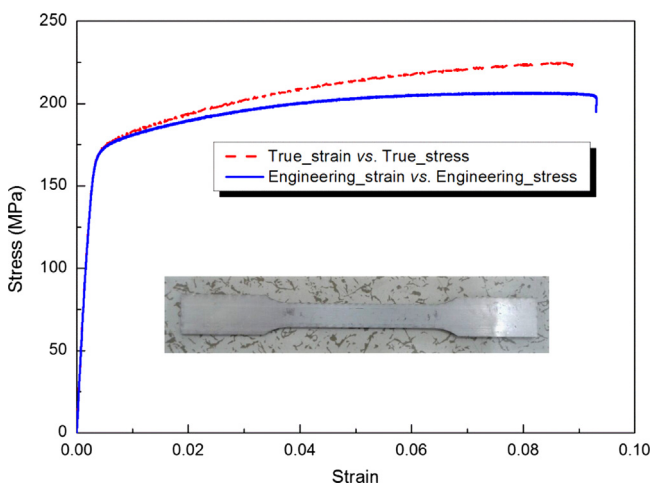

Fig. 6. Tensile specimen and stress–strain curves of AA6063-T5.

the first peak, but has slightly higher values for the rest of the peaks during the subsequent folding. This discrepancy may be caused by the trigger placements in the FE model that actually weaken the initial stiffness of the tube and consequently decrease the first peak force in the simulation. In addition, the existence of imperfections in the physical specimen, which are very difficult to be properly considered in FE modeling, is another reason. Overall, the numerical modeling technique adopted here is considered sufficiently accurate and will be applied to the subsequent study.

3. Numerical analysis of crashworthiness

3.1. Crashworthiness criteria

To systematically study the crashing behaviors of the FGT multi-cell structures, it is essential to define the crashworthiness indicators. Many different indicators have been proposed to evaluate the crashing characteristics and energy absorption capabilities of different structures [35–38]. Of these indicators, the

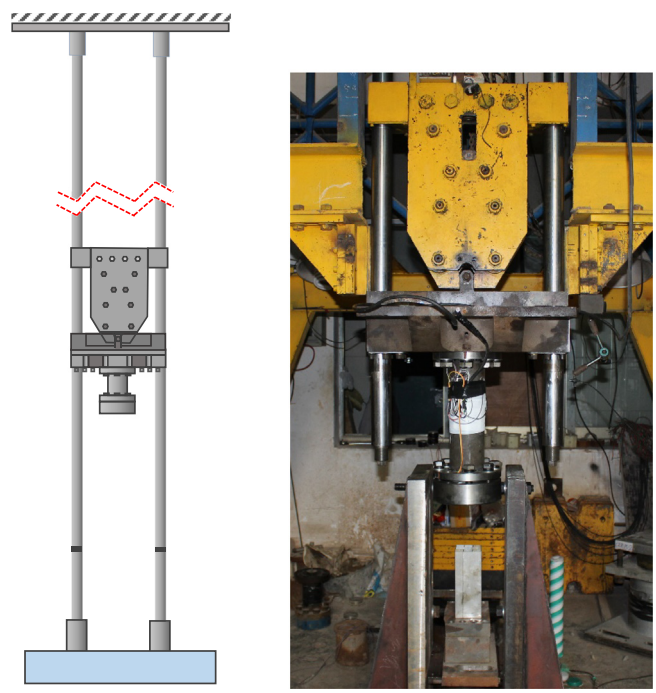

Fig. 7. Dynamic impact experimental setup.

specific energy absorption (*SEA*) is widely used to estimate the energy absorption efficiency of a given structural mass (M) as

$$SEA = \frac{EA}{M} \tag{7}$$

where EA is the total absorbed energy during crashing, which can be calculated as

$$EA = \int_0^{\delta} F(x)dx \tag{8}$$

where $F(x)$ is the impact force in the axial direction and δ *is* the crash displacement. Obviously, a higher *SEA* value indicates a higher capability and efficiency of energy absorption.

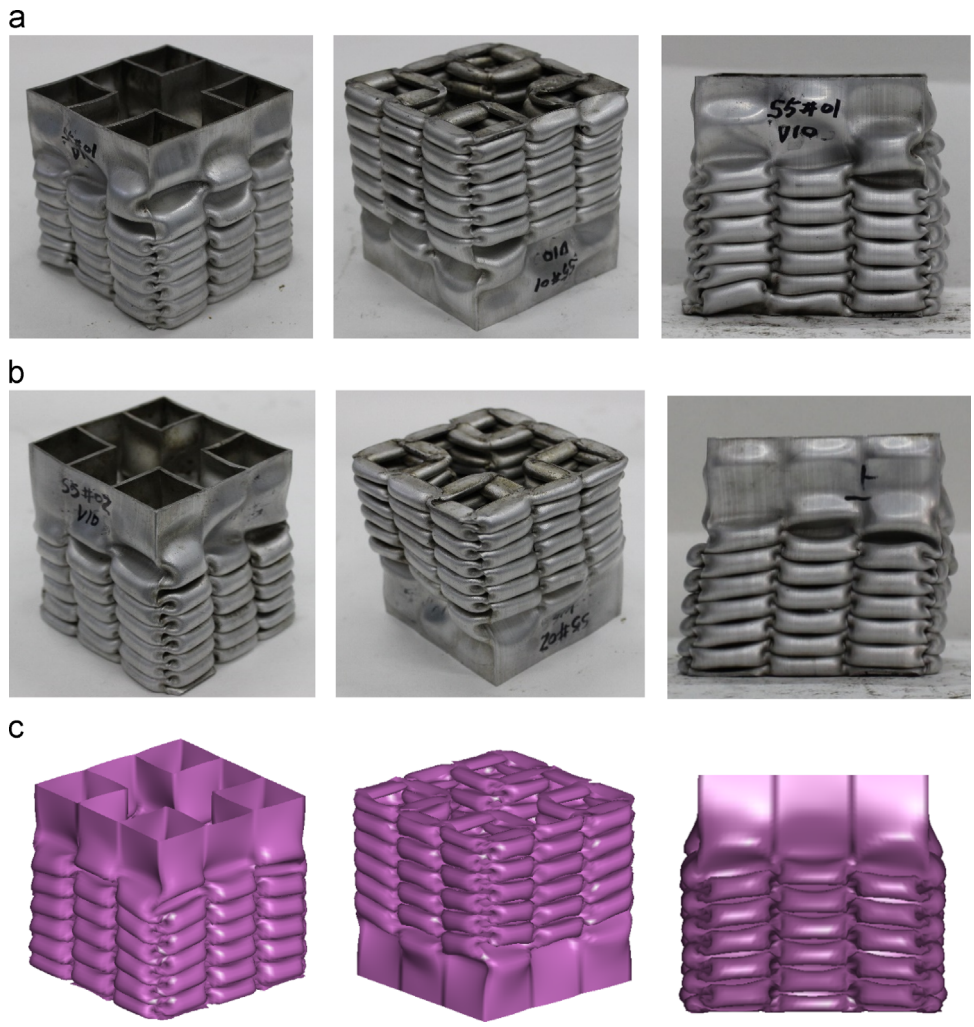

Fig. 8. Comparison of the deformation modes between the experimental and numerical results: (a) dynamic axial impact test-1; (b) dynamic axial impact test-2; and (c) numerical results.

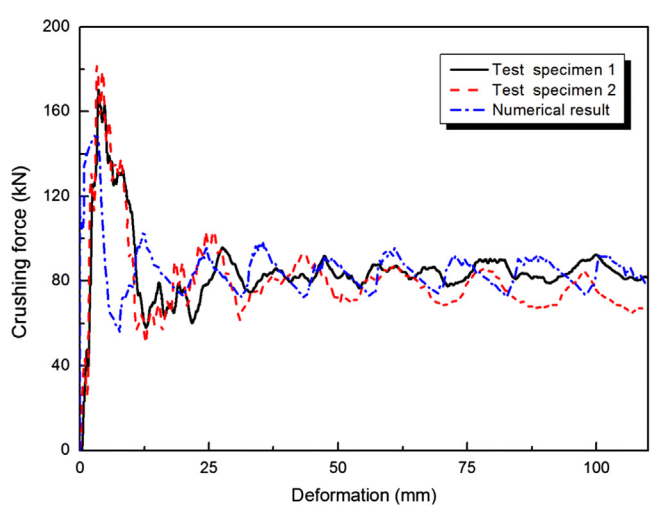

Fig. 9. Comparison of crashing force between experimental and numerical results.

Another indicator is the crash force efficiency (*CFE*) or its reciprocal load ratio (*LR*), given as

$$CFE = \frac{F_{avg}}{F_{max}} \times 100\% \tag{9}$$

$$LR = \frac{F_{max}}{F_{avg}} \times 100\% \tag{10}$$

where F_{max} is the maximum impact force because it represents another critical indicator to the occupant survival rate because a large impact force often leads to a high deceleration and severe injury or even death of the occupant. F_{avg} is the mean crash force, which is calculated by dividing the total energy absorption by the corresponding crushing displacement δ:

$$F_{avg} = \frac{EA}{\delta} \tag{11}$$

In this study, the crashworthiness performances were assessed for the same crash displacement ($\delta = 110$ mm herein) for all tubes, which was commonly used by other researchers [39–42].

3.2. Response surface modeling

To investigate the influence of thickness gradients on the crashworthiness performance, sampling points were generated uniformly over a 3D space of gradient parameters n_1, n_2 and n_3 by using a full factorial design with five levels for each gradient parameter. Then, these sample data were used to approximate *EA* and F_{max}.

To compare the crashworthiness of FGT multi-cell tubes and their counterparts with uniform thickness (UT), each UT multi-cell tube is considered to have the same mass as the corresponding FGT tube at the sample points by assigning a uniform thickness

Table 1
Modeling accuracy of the response surface models.

		Order	R^2	e_{max} (%)	e_{avg} (%)
Gradient	*EA*	Linear	0.9741	7.88	3.10
		Quadratic	0.9749	12.25	3.06
		Cubic	**0.9949**	**3.20**	1.25
		Quartic	0.9947	3.36	**1.20**
	F_{max}	Linear	0.9894	4.68	1.27
		Quadratic	0.9887	5.43	1.33
		Cubic	0.9995	1.04	**0.29**
		Quartic	**0.9995**	**0.77**	0.32
Uniform	*EA*	Linear	0.9902	11.96	1.99
		Quadratic	0.9890	13.04	2.18
		Cubic	**0.9996**	**1.76**	0.50
		Quartic	0.9995	1.82	**0.50**
	F_{max}	Linear	0.9907	6.14	1.36
		Quadratic	0.9904	6.27	1.39
		Cubic	0.9998	0.42	0.22
		Quartic	**0.9998**	**0.39**	**0.22**

based on Eq. (12). Therefore, the response surface models of the *EA* and F_{max} for uniform structures can be established in terms of n_1, n_2 and n_3.

$$\begin{aligned} t_u &= \frac{1}{40L}\left(16\int_0^{L/6} t_1(x_1,n_1)dx_1 + 8\int_0^{L/6} t_2(x_2,n_2)dx_2 \right. \\ &\quad \left. +16\int_0^{L/6} t_3(x_3,n_3)dx_3\right) \\ &= 0.4\left(t_{max} - \frac{t_{max}-t_{min}}{10^{n_1}+1}\right) + 0.2\left(t_{max} - \frac{t_{max}-t_{min}}{10^{n_2}+1}\right) \\ &\quad +0.4\left(t_{max} - \frac{t_{max}-t_{min}}{10^{n_3}+1}\right) \end{aligned} \tag{12}$$

Ten additional points were generated randomly in the design space to examine the accuracies of different orders of RSMs. Three error metrics, R-square (R^2), maximum relative error (e_{max}) and average relative error (e_{avg}), are adopted as follows:

$$R^2 = 1 - \sum_{i=1}^{q}(y_i - \hat{y}_i)^2 / \sum_{i=1}^{q}(y_i - \bar{y})^2 \tag{13}$$

$$e_{max} = \max_{i\in\{1,\ldots,q\}}\left(|y_i - \hat{y}_i|/|y_i|\right) \tag{14}$$

$$e_{avg} = \frac{1}{q}\sum_{i=1}^{q}\left(|y_i - \hat{y}_i|/|y_i|\right) \tag{15}$$

where y_i denotes the *exact* (FE) function value for the examination point i (normally different from the sample point), $\hat{y}_i$ is the corresponding surrogate value, $\bar{y}$ is the mean of y_i, and q is the number of examination points.

Table 1 summarizes the results of the accuracy assessment for the FGT and UT structures. Clearly, the values of R^2 are all close to 1 and the values of e_{max} and e_{avg} are within 8%. However, no single response surface model performed well for all crashworthiness indicators, and the RSM accuracy may not increase by choosing a higher order model. Thus, the selected orders of the RSMs are highlighted in Table 1 for subsequent optimizations, and their expressions are given in Eqs. (16)–(19), where superscripts *G* and *U* represent the FGT and UT multi-cell tubes, respectively. Based on Eq. (7), the *SEA* can be calculated using Eq. (20), where *A* and ρ are the total area of the walls and density of aluminum, respectively.

$$\begin{aligned} F^G_{\max}(n_1,n_2,n_3) &= 137.4090 + 32.71930n_1 + 15.4635n_2 \\ &\quad +27.8681n_3 + 1.0131n_1n_2 \\ &\quad +1.5061n_2n_3 + 0.9900n_1n_3 + 0.2054n_1^2 + 0.5474n_2^2 \\ &\quad +2.7585n_3^2 - 10.0051n_1^3 - 4.5190n_2^3 - 8.3596n_3^3 \\ &\quad -0.8477n_1^4 - 0.2640n_2^4 \\ &\quad -1.8502n_3^4 \end{aligned} \tag{16}$$

$$\begin{aligned} EA^G(n_1,n_2,n_3) &= 9.5158 + 2.2870n_1 + 0.8224n_2 + 3.6508n_3 \\ &\quad -0.1996n_1n_2 + 0.0463n_2n_3 + 0.2490n_1n_3 + 0.0127n_1^2 \\ &\quad +0.2211n_2^2 - 0.2738n_3^2 \\ &\quad -0.7889n_1^3 - 0.2464n_2^3 - 1.2545n_3^3 \end{aligned} \tag{17}$$

$$\begin{aligned} F^U_{max}(n_1,n_2,n_3) &= 138.1987 + 32.9659n_1 + 16.4822n_2 + 32.9658n_3 \\ &\quad +0.2325n_1n_2 + 0.1564n_2n_3 + 0.3291n_1n_3 \\ &\quad +0.0796n_1^2 + 0.1564n_2^2 + 0.2325n_3^2 \\ &\quad -8.7673n_1^3 - 4.3983n_2^3 - 8.7673n_3^3 - 0.1017n_1^4 \\ &\quad -0.0220n_2^4 + 0.1016n_3^4 \end{aligned} \tag{18}$$

$$\begin{aligned} EA^U(n_1,n_2,n_3) &= 8.1407 + 2.8301n_1 + 1.4192n_2 + 2.8307n_3 \\ &\quad +0.0390n_1n_2 + 0.0593n_2n_3 + 0.1121n_1n_3 \\ &\quad +0.0032n_1^2 + 0.0589n_2^2 + 0.0382n_3^2 \\ &\quad -0.7388n_1^3 - 0.3676n_2^3 - 0.7393n_3^3 \end{aligned} \tag{19}$$

$$SEA^{G(U)}(n_1,n_2,n_3) = EA^{G(U)}/(t_u \cdot A \cdot \rho) \tag{20}$$

3.3. Effect of the thickness gradients

3D response surfaces (RS) of the crashworthiness indicators are plotted in Figs. 10–13. From Fig. 10, it can be observed that F_{max} increases monotonically as n_1, n_2 and n_3. This result occurs mainly because the intermediate thicknesses (between t_{min} and t_{max}) in the corresponding region (as shown in Fig. 4) as the gradient parameters increase, which strengthens the tube structure. Therefore, the values of *EA* and *SEA* increase as the gradient parameters (Figs. 11 and 12). Furthermore, it is advantageous to increase the gradient parameter n_2 to yield a higher *CFE*, as shown in Fig. 13. While increasing the gradient parameters seems to be an effective way to increase *EA* and *SEA*, it would result in an undesirable increase in F_{max}.

3.4. Comparison of the FGT and UT multi-cell tubes

To compare the crashworthiness of the FGT multi-cell tubes and their counterparts with uniform thickness (UT), the response surfaces of the UT structures are plotted in Figs. 10–13. From Fig. 10 when n_2 is smaller, the FGT tubes have slightly larger values of F_{max} than the UT tubes; while when n_2 is larger, the FGT tubes have slightly smaller values of F_{max}. Overall, no significant difference in F_{max} is observed between the FGT and UT structures. In regards to *EA* and *SEA*, the FGT tubes outperform the UT tubes for a majority of the space as displayed in Figs. 11 and 12. But when $n_1 = n_3 = 1$ and $n_2 = -1$, the UT tubes perform better than their FGT counterparts. From Fig. 13, the FGT tubes are always preferable to the UT tubes in terms of *CFE*.

4. Multiobjective optimization of the FGT multi-cell tubes

4.1. Optimization methodology

4.1.1. Definition of the optimization problem

Based on the previous parametric analysis, it is clear that the gradient parameters largely affect the crashworthiness of the FGT multi-cell tubes, but it is unknown how to determine the appropriate gradients to achieve the best possible performance, which is the main task of the rest of this study. As an energy absorber, the tube structure is expected to absorb as much impact energy per unit mass as possible. Thus, the *SEA* should be the objective function to

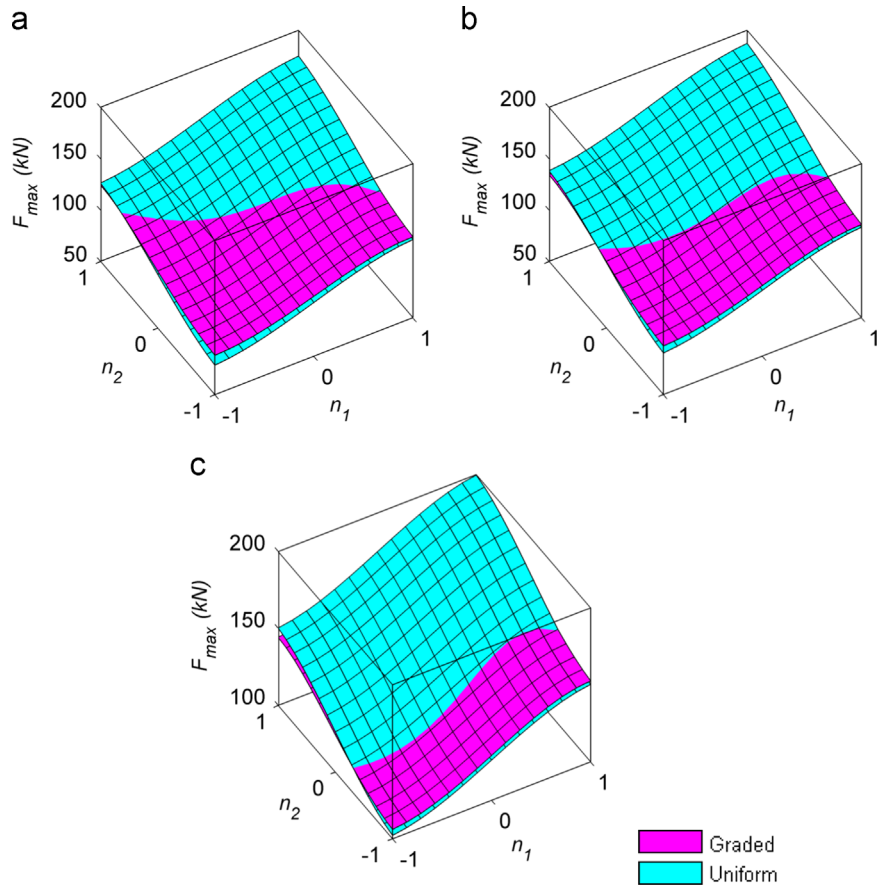

Fig. 10. 3D response surfaces of F_{max}: (a) $n_3=-1$; (b) $n_3=0$; and (c) $n_3=1$.

maximize. Furthermore, F_{max} of the structure is another indicator of the safety of the occupants and should be minimized. Therefore, we formulated a multiobjective optimization problem in Eq. (21) to determine the optimum gradient configurations for these two design criteria as,

$$\begin{cases} \min & F_{max}{}^{G(U)}, -SEA^{G(U)} \\ \text{s.t.} & -1 \le n_1, n_2, n_3 \le 1 \end{cases} \tag{21}$$

4.1.2. Multiobjective particle swarm optimization (MOPSO)

The particle swarm optimization (PSO) algorithm [43] is a relatively new heuristic approach inspired by the choreography of a flock of birds. An extended version of the PSO, the multiobjective particle swarm optimization (MOPSO) algorithm, is characterized by fast convergence and a well-distributed Pareto frontier compared with other multiobjective optimization algorithms such as NSGA-II[44], PEAS and microGA [45,46]. Note that MOPSO has been employed successfully to solve a series of design problems, such as the crashworthiness of foam filled structures [34,35,47]. In this paper, the MOPSO proposed by Coello et al. [45] is utilized to handle the multiobjective problem defined in Eq. (21). The algorithm works as follows:

(1) Initialize the position $\mathbf{x}_i$ and velocity $\mathbf{v}_i$ of each particle.

(2) Evaluate each particle and store the positions of the non-dominated particles in the repository.

(3) Generate hypercubes of the explored search space, and then locate the particles.

(4) Initialize the memory of each particle:

$$\mathbf{p}_i = \mathbf{x}_i \tag{22}$$

(5) Do the following if the maximum number of iterations has not been reached:

(a) Compute the velocity of each particle by

$$\mathbf{v}_{i+1} = w\mathbf{v}_i + c_1 r_1(\mathbf{p}_i - \mathbf{x}_i) + c_2 r_2(\mathbf{p}_g - \mathbf{x}_i) \tag{23}$$

where w is the inertial weight; r_1 and r_2 are random numbers between 0 and 1; c_1 and c_2 are the personal and global learning coefficients, respectively; $\mathbf{p}_i$ is the best position that the particle i has had so far; and $\mathbf{p}_g$ is a value taken from the repository.

(b) Compute the new positions of the particles by adding the velocity calculated from the previous step:

$$\mathbf{x}_{i+1} = \mathbf{x}_i + \mathbf{v}_{i+1}. \tag{24}$$

(c) Perform a boundary treatment to keep the particles within the search space.

(d) Evaluate each particle and update the contents of the repository together with the geographical representation of the particles within the hypercubes.

(e) Update the $\mathbf{p}_i$ of each particle.

(f) Increase the iteration counter and return to the beginning of step (5).

4.2. Results and discussion

Fig. 14 compares the Pareto frontiers of the FGT and UT multi-cell tubes; the MOPSO parameters for solving the multiobjective optimization problems are summarized in Table 2. The Pareto optimal frontiers provide designers with a wide spectrum of solutions over the design space. Most importantly, when the optimized conventional UT tubes are replaced by the optimized FGT tubes, the Pareto frontier indicates considerably better

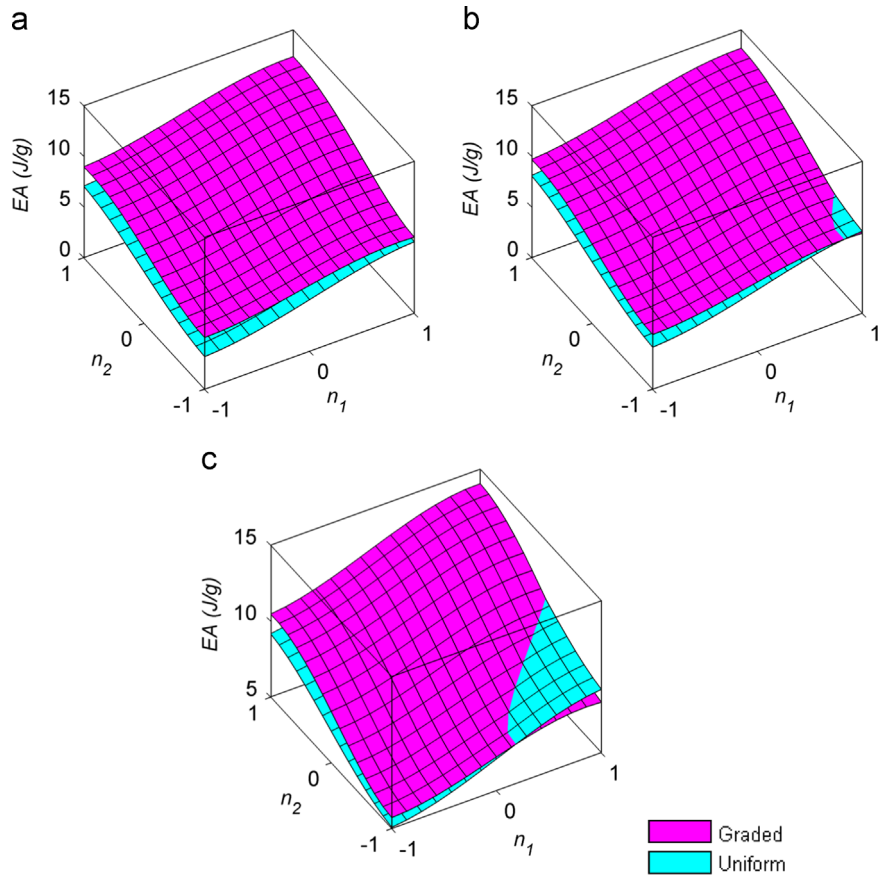

Fig. 11. 3D response surfaces of *EA*: (a) $n_3=-1$; (b) $n_3=0$; and (c) $n_3=1$.

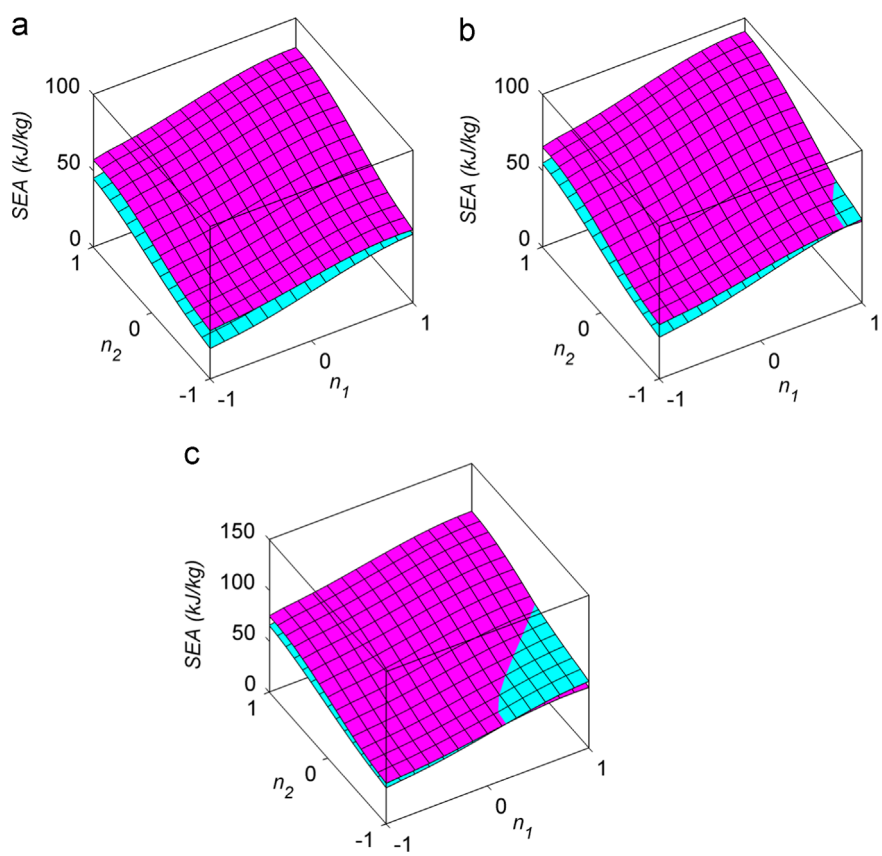

Fig. 12. 3D response surfaces of SEA: (a) $n_3=-1$; (b) $n_3=0$; and (c) $n_3=1$.

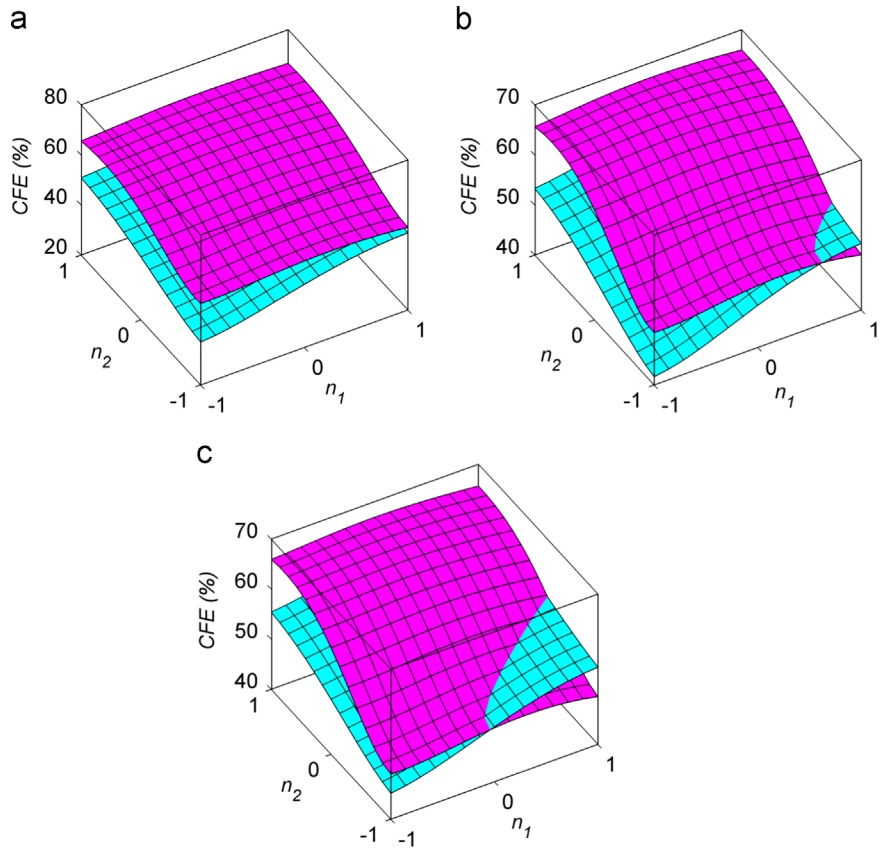

Fig. 13. 3D response surfaces of CFE: (a) $n_3=-1$; (b) $n_3=0$; and (c) $n_3=1$.

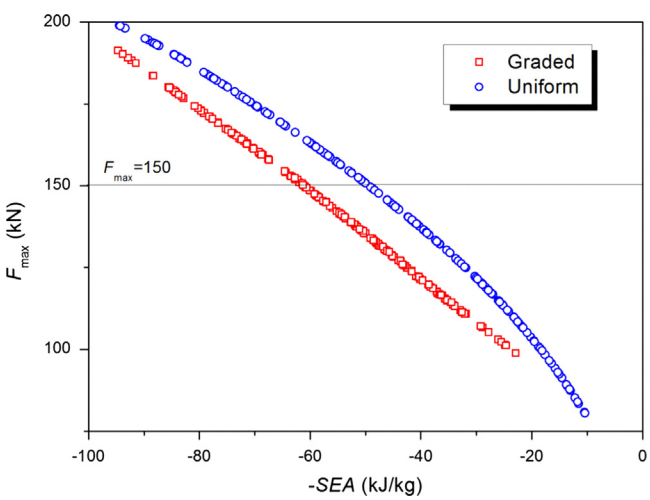

Fig. 14. Pareto frontiers of the FGT and UT multi-cell tubes.

performance for both F_{max} and *SEA*. In other words, the FGT multi-cell tubes enhance the *SEA* and lower the F_{max} concurrently.

Fig. 15 depicts the distribution of Pareto optimum solutions of the FGT multi-cell tubes in the design space. To achieve a wide range of crashworthiness performances, each of the design variables (i.e., gradient parameters) spreads over their corresponding dimensions of the design space. Interestingly, all of the optimums are located around the diagonal line of $n_1=n_2$, which indicates that similar values of gradient parameters in the outer walls are more likely to yield optimal performance. Moreover, the optimums also have values of $n_3>n_1$ and $n_3>n_2$, which indicates stronger internal ribs improve the performance of the FGT multi-cell tubes.

Table 2
Settings of the MOPSO.

MOPSO parameter name	Value
Population size	100
No. of generations	200
External archive size	200
Inertial weight	0.73
Personal learning coefficient	1.50
Global learning coefficient	1.50

In real-life applications, F_{max} is often required to remain below a certain threshold for the occupant's safety. In this study, if we constrain $F_{max}\leq 150$ kN for a quantitative comparison between FGT and UT multi-cell structures, the optimal solutions can be simply selected from the intersection between the Pareto frontiers and the horizontal line of $F_{max}=150$ kN. Table 3 lists the two specific optimums where the surrogate models were also checked against the FE analyses. It is seen that the RS model can predict the actual performance with fairly high accuracy. Furthermore, while these two designs develop the same first peak force (F_{max}), the crashing force of the FGT multi-cell tube is maintained at a higher level during the subsequent deformation, as seen in Fig. 16, in which the shaded area between these two curves is the additional energy absorbed by the FGT structure. As a result, the *SEA* of the FGT structure increases to 58.94 kJ/kg by 19.51%.

5. Conclusions

To explore the dynamic crashing behavior of multi-cell tubes with a functionally graded thickness (FGT), which can be

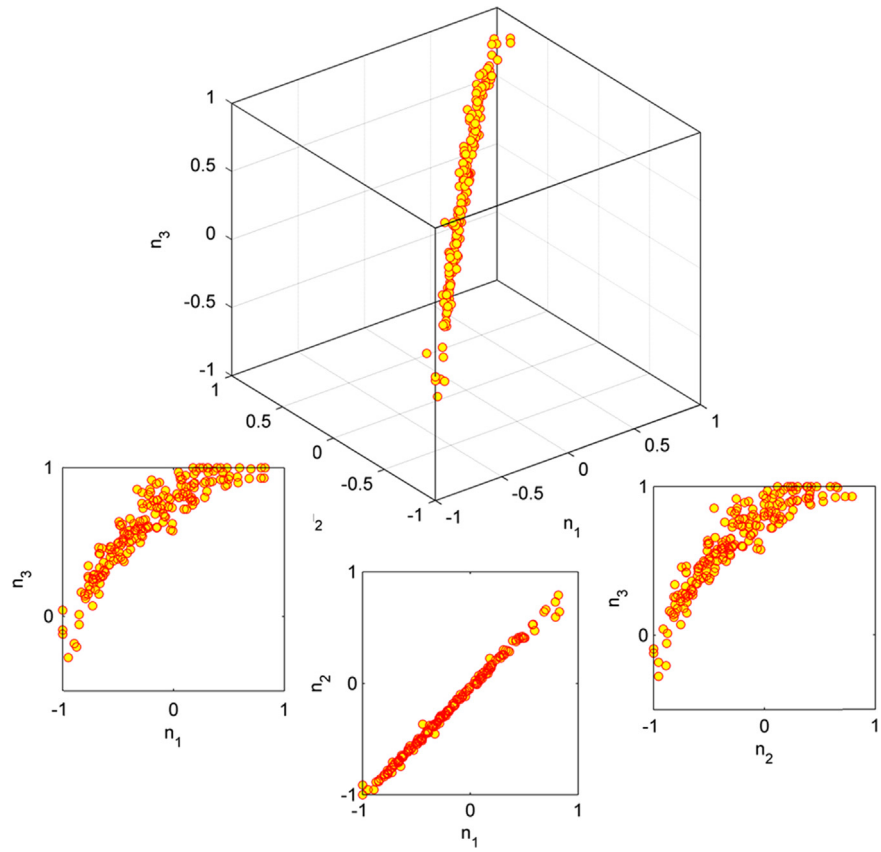

Fig. 15. Distribution of Pareto solutions of the FGT multi-cell tubes.

Table 3
Optimal solutions ($F_{max} \leq 150$ kN).

	UT	FGT
n_1	0.1124	−0.0821
n_2	0.1550	−0.1274
n_3	0.1550	0.6738
F_{max} (kN)		
Eq. (16)/(18)	149.53	149.78
FE	149.83	149.16
Error (%)	−0.20	0.42
SEA (kJ/kg)		
Eq. (20)	49.05	60.90
FE	49.32	58.94
Error (%)	−0.56	3.32

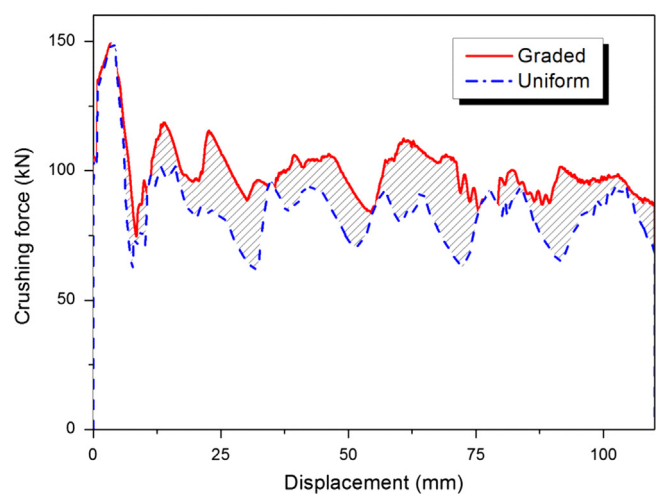

Fig. 16. Crushing force of the optimal structures.

fabricated by a dedicated extrusion process, a numerical model was constructed using the non-linear finite element (FE) code LS-DYNA. The FE model was then validated for the deformation pattern, impact force curve and energy curve using experimental data. In the numerical study, it was discovered that the FGT multi-cell tubes provide better specific energy absorption (*SEA*), energy absorption (*EA*) and crash force efficiency (*CFE*) as well as similar values of the maximum impact force (F_{max}) than the uniform thickness (UT) counterpart. Furthermore, the gradient parameters of the wall thickness in the FGT multi-cell tubes affect the crashworthiness performance significantly.

To seek an optimal design for crashworthiness, multiobjective optimizations were performed to simultaneously minimize the F_{max} and maximize the *SEA*. The response surface model (RSM) and multiobjective particle optimization (MOPSO) algorithm were integrated to perform the optimizations. The results showed that the optimal FGT multi-cell tube yielded much better Pareto frontiers than the optimal UT counterparts. Moreover, similar gradients were recommended to achieve better crashworthiness because this leads to a better interaction between the different regions of the section configuration. In conclusion, the novel structure of the FGT multi-cell tube is worth studying and could be an ideal energy absorber in engineering applications.

Acknowledgments

This work was supported by the National Natural Science Foundation of China (51575172) and the Doctoral Fund of the

Ministry of Education of the People's Republic of China (20120161120005). The first author is a recipient of doctoral scholarships from both the China Scholarship Council (CSC) and the University of Sydney.

References

[1] Marsolek J, Reimerdes HG. Energy absorption of metallic cylindrical shells with induced non-axisymmetric folding patterns. Int J Impact Eng 2004;30:1209–23.
[2] De Santis F. The modelling of the vehicle frontal structure and the numerical simulation of the crash-test [Master's thesis]. Torino, Italy: Politecnico di Torino, Facoltá di Ingegneria, Corso di specializzazione in Ingegneria Meccanica; 1996.
[3] Alexander J. An approximate analysis of the collapse of thin cylindrical shells under axial loading. Q J Mech Appl Math 1960;13:10–5.
[4] Wierzbicki T, Abramowicz W. On the crushing mechanics of thin-walled structures. J Appl Mech—Trans ASME 1983;50:727–34.
[5] Abramowicz W, Jones N. Dynamic axial crushing of square tubes. Int J Impact Eng 1984;2:179–208.
[6] Abramowicz W, Jones N. Dynamic progressive buckling of circular and square tubes. Int J Impact Eng 1986;4:243–70.
[7] Meng Q, Al-Hassani STS, Soden PD. Axial crushing of square tubes. Int J Mech Sci 1983;25:747–73.
[8] Andrews KRF, England GL, Ghani E. Classification of the axial collapse of cylindrical tubes under quasi-static loading. Int J Mech Sci 1983;25:687–96.
[9] Mamalis AG, Johnson W. The quasi-static crumpling of thin-walled circular cylinders and frusta under axial compression. Int J Mech Sci 1983;25:713–32.
[10] Kim HS. New extruded multi-cell aluminum profile for maximum crash energy absorption and weight efficiency. Thin-Walled Struct 2002;40:311–27.
[11] Abramowicz W, Wierzbicki T. Axial crushing of multicorner sheet metal columns. J Appl Mech 1989;56:113–20.
[12] Zhang X, Cheng GD, Zhang H. Theoretical prediction and numerical simulation of multi-cell square thin-walled structures. Thin Walled Struct 2006;44:1185–91.
[13] Hou SJ, Li Q, Long SY, Yanga XJ, Li W. Multiobjective optimization of multi-cell sections for the crashworthiness design. Int J Impact Eng 2008;35:1355–67.
[14] Qi C, Yang S, Dong F. Crushing analysis and multiobjective crashworthiness optimization of tapered square tubes under oblique impact loading. Thin-Walled Struct 2012;59:103–19.
[15] 〈http://www.alueurope.eu/wp-content/uploads/2011/12/4_AAM_Crash-management-systems1.pdf〉.
[16] Zhang X, Wen Z, Zhang H. Axial crushing and optimal design of square tubes with graded thickness. Thin-Walled Struct 2014;84:263–74.
[17] Fang J, Gao Y, Sun G, Xu C, Li Q. Fatigue optimization with combined ensembles of surrogate modeling for a truck cab. J Mech Sci Technol 2014;28:1–9.
[18] Sun G, Tian X, Fang J, Xu F, Li G, Huang X. Dynamical bending analysis and optimization design for functionally graded thickness (FGT) tube. Int J Impact Eng 2014.
[19] Zhang X, Zhang H, Wen Z. Axial crushing of tapered circular tubes with graded thickness. Int J Mech Sci 2015;92:12–23.
[20] Song XG, Jung JH, Son HJ, Park JH, Lee KH, Park YC. Metamodel-based optimization of a control arm considering strength and durability performance. Comput Math Appl 2010;60:976–80.
[21] Yang RJ, Wang N, Tho CH, Bobineau JP. Metamodeling development for vehicle frontal impact simulation. J Mech Design 2005;127:1014–20.
[22] Song X, Sun G, Li G, Gao W, Li Q. Crashworthiness optimization of foam-filled tapered thin-walled structure using multiple surrogate models. Struct Multidiscip Optim 2013;47:221–31.
[23] Fang J, Gao Y, Sun G, Li Q. Development of a novel identification platform for automotive dampers. Int J Veh Design 2014;66:272–96.
[24] Fang J, Gao Y, Sun G, Xu C, Li Q. Multiobjective robust design optimization of fatigue life for a truck cab. Reliabil Eng Syst Saf 2014.
[25] Fang J, Gao Y, Sun G, Xu C, Zhang Y, Li Q. Optimization of spot-welded joints combined artificial bee colony algorithm with sequential kriging optimization, Advances in. Mech Eng 2014 2014.
[26] Sun G, Li G, Zhou S, Li H, Hou S, Li Q. Crashworthiness design of vehicle by using multiobjective robust optimization. Struct Multidiscip Optim 2011;44:99–110.
[27] Sun G, Li G, Gong Z, Cui X, Yang X, Li Q. Multiobjective robust optimization method for drawbead design in sheet metal forming. Mater Design 2010;31:1917–29.
[28] Liao X, Li Q, Yang X, Li W, Zhang W. A two-stage multi-objective optimisation of vehicle crashworthiness under frontal impact. Int J Crashworth 2008;13:279–88.
[29] Hou S, Li Q, Long S, Yang X, Li W. Design optimization of regular hexagonal thin-walled columns with crashworthiness criteria. Finite Elem Anal Design 2007;43:555–65.
[30] Fang J, Gao Y, Sun G, Li Q. Multiobjective reliability-based optimization for design of a vehicle door. Finite Elem Anal Design 2013;67:13–21.
[31] Hallquist JO. LS-DYNA theory manual, vol. 3. Livermore Software Technology Corporation; 2006.
[32] Belytschko T, Lin JI, Chen-Shyh T. Explicit algorithms for the nonlinear dynamics of shells. Comput Methods Appl Mech Eng 1984;42:225–51.
[33] Mamalis AG, Manolakos DE, Ioannidis MB, Kostazos PK. Numerical simulation of thin-walled metallic circular frusta subjected to axial loading. Int J Crashworth 2005;10:505–13.
[34] Fang J, Gao Y, Sun G, Zhang Y, Li Q. Parametric analysis and multiobjective optimization for functionally graded foam-filled thin-wall tube under lateral impact. Comput Mater Sci 2014;90:265–75.
[35] Sun G, Li G, Hou S, Zhou S, Li W, Li Q. Crashworthiness design for functionally graded foam-filled thin-walled structures. Mater Sci Eng: A 2010;527:1911–9.
[36] Guler MA, Cerit ME, Bayram B, Gerceker B, Karakaya E. The effect of geometrical parameters on the energy absorption characteristics of thin-walled structures under axial impact loading. Int J Crashworth 2010;15:377–90.
[37] Zheng G, Wu S, Sun G, Li G, Li Q. Crushing analysis of foam-filled single and bitubal polygonal thin-walled tubes. Int J Mech Sci 2014;87:226–40.
[38] Costas M, Díaz J, Romera L, Hernández S. A multi-objective surrogate-based optimization of the crashworthiness of a hybrid impact absorber. Int J Mech Sci 2014;88:46–54.
[39] Yang S, Qi C. Multiobjective optimization for empty and foam-filled square columns under oblique impact loading. Int J Impact Eng 2013;54:177–91.
[40] Song J, Guo F. A comparative study on the windowed and multi-cell square tubes under axial and oblique loading. Thin Wall Struct 2013;66:9–14.
[41] Yin H, Wen G, Fang H, Qing Q, Kong X, Xiao J, Liu Z. Multiobjective crashworthiness optimization design of functionally graded foam-filled tapered tube based on dynamic ensemble metamodel. Mater Design 2014;55:747–57.
[42] Zarei H, Kröger M. Crashworthiness optimization of empty and filled aluminum crash boxes. Int J Crashworth 2007;12:255–64.
[43] Eberhart R, Kennedy J. A new optimizer using particle swarm theory. In: Proceedings of the sixth international symposium on Micro machine and Human Science, 1995 (MHS'95). IEEE; 1995. p. 39–43.
[44] Liao X, Li Q, Yang X, Zhang W, Li W. Multiobjective optimization for crash safety design of vehicles using stepwise regression model. Struct Multidiscip Optim 2008;35:561–9.
[45] Coello CAC, Pulido GT, Lechuga MS. Handling multiple objectives with particle swarm optimization. IEEE Trans Evol Comput 2004;8:256–79.
[46] Raquel CR, Naval Jr PC. An effective use of crowding distance in multiobjective particle swarm optimization. In: Proceedings of the 2005 conference on genetic and evolutionary computation. ACM; 2005. p. 257–64.
[47] Fang J, Gao Y, Sun G, Zhang Y, Li Q. Crashworthiness design of foam-filled bitubal structures with uncertainty. Int J Non-Linear Mech 2014;67:120–32.

View publication stats